The International Journal of Advanced Manufacturing Technology
https://doi.org/10.1007/s00170-020-06443-y

ORIGINAL ARTICLE

Buckling and wrinkling of rectangular hollow sections curved in three-point-roll bending

Roy Cornelissen [1,2] · Johan Maljaars [1,3] · Hèrm Hofmeyer [1]

Received: 29 April 2020 / Accepted: 1 December 2020

Abstract
Curved aluminium extrusions are applied in a wide range of industrial applications. Because extrusions are initially straight, an additional process is required to curve the product. Undesired wrinkling of the plate part at the inner radius is frequently observed during the curving process. Wrinkling has already been extensively studied for the rotary-draw bending process. This paper aims at predicting the conditions for which wrinkling of a hollow section can occur during the three-point-roll bending process. It is shown that the most important condition for wrinkling is that buckling of the compressed plate part at the inner radius occurs. An analytical prediction model for buckling is presented, which predicts the critical bending radius as a function of the plate slenderness. The analytical model is validated with a finite element model, which in turn is validated with an experiment. Both the finite element model and the experiment confirm that wrinkling does not occur if the applied radius exceeds the model predicted critical radius.

Keywords Three-point-roll bending · Curving · Local buckling · Wrinkling · Process simulation

1 Introduction

Aluminium alloys are well known for their excellent strength-to-weight ratio, and are therefore widely applied in the transport and construction industries. These industries often demand casted and extruded aluminium products of various shapes that should meet high standards with respect to mechanical and visual properties. An extruded product is initially straight, due to its production process. An additional process therefore is required if the final product needs to be curved. The two most often applied curving processes are as follows: (a) rotary-draw bending (RDB, Fig. 1); and (b) three-point-roll bending (TPRB, Fig. 2). Obviously, these procedures take place near the end of the production process. Therefore, the parameters of these curving procedures determine to a large extent the quality of the finalised product. One of these qualities, surface quality, is related to the presence and magnitude of scratches and cracks and to (excessive) deformation and wrinkling, the latter being the subject of this paper.

Wrinkling has been mainly studied for RDB. An RDB machine (RDM) consists of the components as given in Fig. 1: (1) pressure die, (2) wiper die, (3) mandrel, (4) bending die, (5) clamping die, (6) flexible mandrel balls and an optional (7) boosting die. RDB provides a product with a local curvature due to a rotational movement ω_{draw} of the bending die. A boosting die supports the curving process by performing an actuated movement v_{boost} in the direction aligned with the movement of the product caused by ω_{draw}.

Experimental, analytical and numerical studies have been conducted regarding several aspects involved in RDB, in order to gain control over the surface quality. Common practice in most studies has been to threat a single aspect of the curving process, resulting in the following fields of study: mechanics involved in curving, spring back, machine settings, residual stresses, strain hardening and damage. Zhu et al. [1] observed that wrinkling starts in the part of the section in front of the bending die, i.e., before it is in contact with the die. Friction between the bending die and the section was found to be of importance for wrinkling. He et al. [2] conducted a study

✉ Johan Maljaars
j.maljaars@tue.nl

[1] Department of the Built Environment, Eindhoven University of Technology, Eindhoven, The Netherlands

[2] Kersten Europe, Piet van Elsstraat 7, NL 5861 AW Wanssum, The Netherlands

[3] Department of Structural Reliability, TNO, Delft, The Netherlands

Published online: 06 January 2021

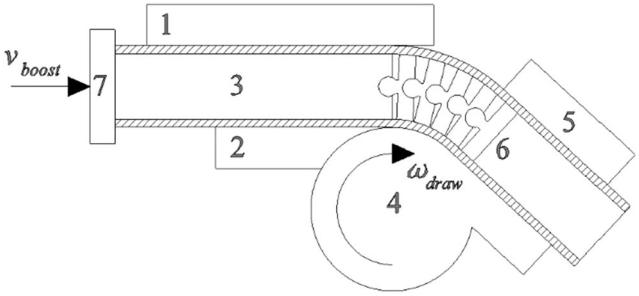

Fig. 1 Rotary-draw bending (RDB) configuration

including various process parameters, considering the coefficient of friction (COF) and the lack of fit (LOF) between the different parts of the RDM and the effect of the ratio between the wall thickness over the bending radius on these COF and LOF coefficients. The obtained observations are summarized in Table 1, where "negative" or "positive" refers to a deterioration or improvement, respectively, of the (wrinkling related) surface quality. In addition, it was observed that the effects of the coefficients are amplified for an increasing plate slenderness.

Xiao et al. [3] studied the combined effects of the process parameters given in Table 1 on wrinkling and wall thinning or thickening of a double-ridged wrought copper brass hollow section by using a grey relational analysis. The governing parameters for the studied effects are indicated in Table 1 by a [3].

Chen and Zhang [4] studied the effect of the bending velocity on the wrinkling of stainless steel and aluminium CHS. They observed that the interaction between the different parts of the RDM and the section hinders material flow at higher bending speeds. Consequently, material flow lags behind the speed of the process. This causes material to accumulate in front of the bending die, which in turn results into higher magnitudes of wrinkling. Li et al. [5] found that wall thinning and wrinkling is decreased if the bending velocity is controlled by a proper boosting velocity, but this effect depends on the LOF between the mandrel (cores) and section and the LOF between the pressure die and the section.

Table 1 Summary of the influence of the interaction coefficients on the wrinkling of an aluminium circular hollow section (CHS)

Interaction	Effect
LOF between the wiper die and CHS	Negative
LOF between the mandrel (cores) and CHS [3]	Negative
LOF between the bending die and CHS [3]	Positive
LOF between the pressure die and CHS	Positive
Decrease in COF between wiper die and CHS	Negative
Decrease in COF between mandrel and CHS	Negative
Decrease in COF between bending die and CHS	Negative
Decrease in COF between pressure die and CHS	Positive

Safdarian [6] and Fang et al. [7] found that an increase of the extension length of the mandrel, after the bending point, results in an increase in wall thinning and a decrease in wrinkling. Material-related mandrel characteristics are also shown to be important when considering wrinkling during RDB. As an example, Liang et al. [8] found that the rigidity of the mandrel is of influence on the susceptibility of the wrinkling of a steel RHS with an inner core.

The above overview indicates that the process parameters have an important influence on wrinkling. As such, and taking

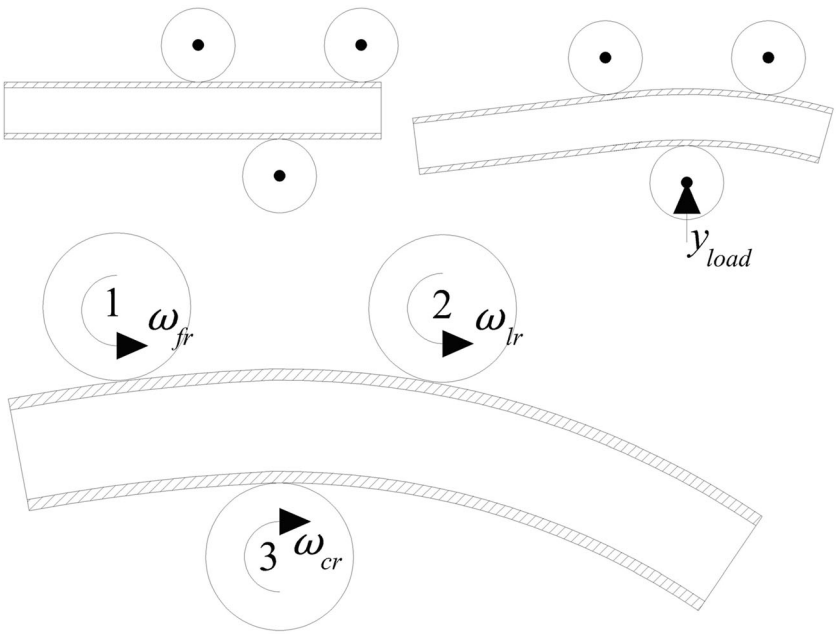

Fig. 2 Three-point-roll bending (TPRB) configuration

into account practical curving conditions, He et al. [2] used a criterion for wrinkling based on the energy method [9]:

$$0.8 < \frac{T}{U_{\min}} < 1.0 \tag{1}$$

where factor 1.0 is the theoretical limit value, considered an upper bound in [2], and the factor 0.8 is a practical lower bound that takes into account the imperfections of the machinery. T is the load potential obtained indirectly via the energy dissipated in plastic deformation (EDPD) at the compressed side of the hollow section, obtained from a finite element (FE) model:

$$T = \sum_{e=1}^{n} \sigma_e \varepsilon_e V_e \tag{2}$$

where n is the number of finite elements in the compressed deformation zone, V_e is the volume of the element, and σ_e and ε_e are its average equivalent stress and strain, respectively. $U_{\min}$ in Eq. (1) is the strain energy (SE) related to the wrinkling of the hollow section. It consists of the following terms:

$$U_{\min} = U_{\text{tube}} + U_{\text{machine}} \tag{3}$$

where U_{tube} is the energy required to initiate plate buckling, and U_{machine} is the work done by the RDM on the hollow section and depends on the LOF.

To develop a decision model for the process parameters that enables rotary draw bending without wrinkling and distortions, the bending limits of CHS have been investigated in Li et al. [10]. To predict wrinkling, thinning and flattening, theoretical models were used, and these were verified with experiments. Subsequently, the theoretical models were used to describe the safe combination of design parameters, taken all three types of failure into account. Specifically for wrinkling, the theoretical model was based on a minimum-energy prediction (Li et al. [11]).

It is also evident from Eq. (2) that the material parameters affect the work done on the section, and many researchers have shown that the material consequently affects wrinkling. Jie et al. [12] studied the effect of material properties on the wrinkling of a rectangular wrought copper brass section, with results according to Table 2 (using a similar setup as Table 1, and with INAS explained hereafter), where K and n are parameters of the so-called Holloman's strain hardening equation:

$$\sigma(\varepsilon_p) = K\varepsilon_p^n \tag{4}$$

where σ is the stress and ε_p is the plastic strain.

Zhao et al. [13] derived an analytically model for the effect of strain hardening on wrinkling of an aluminium rectangular hollow section (RHS) using the principle of stationary potential energy (PE) and Holloman's equation. Similar to [12], it was observed that materials with a high value for K—i.e. a strong material—and a low value for n—i.e. little strain hardening—have poor formability properties. As such, these materials cause concentrated yielding in the section, subsequently increasing the sensitivity to and magnitude of wrinkling deformations. Guangjun et al. [14] found that variations of hardening exponents, thickness anisotropy and the Young's modulus had a large effect on the bending properties, and so on wrinkling. The effect of the anisotropy was also studied in Hasanpour et al. [15] by using the Hill yield locus, with a similar effect on wrinkling as observed in [12]. This effect can be explained by the relationship between anisotropy and lateral contraction, and the fact that during RDB, the dies and mandrel restrain lateral contraction. Note that this is one of the reasons why heat treatment prior to curving can reduce wrinkling, since by the treatment grains with equal multiaxial, properties are formed during recrystallization.

Table 2 Summary of material properties on wrinkling and INAS

Increase of		Wrinkling [12]	INAS [16]
Yield stress	f_0	Negative	-
Strength coefficient	K	Negative	-
Strain hardening index	n	Positive	+
Young's modulus	E	Positive	NC
Normal anisotropy	γ	Negative	-

Another influencing factor on the occurrence and magnitude of wrinkling during RDB, with a significant interaction with the material parameters as well, is the so-called inward neutral axis shift (INAS), which was studied by Li et al. [16]. It was shown that the larger the INAS, the larger the wrinkling distortions become. The effects of material properties on the INAS are shown in Table 2, in which '–' and '+' refer to a smaller and a larger INAS respectively, whereas NC refers to not considered. Considering materials with different yield strength in tension compared to compression, INAS appears to decrease if the ratio between the tensile yield stress and the compressive yield stress increases. The effects of the strength coefficient and normal anisotropy on the INAS increase, whereas the effect of the strain hardening index reduces.

Finally, the section geometry influences the susceptibility to wrinkling. Many researchers have shown that the plate slenderness is of significant importance to wrinkling. For aluminium CHS and RHS respectively, He et al. [2] and Zhao et al. [13] concluded that an increase in plate slenderness causes an increase in the critical radius, which is the largest radius for which the compressed section part wrinkles. The interaction of plate elements is studied by Liu et al. [17] for aluminium RHS and U- and L-shaped sections. They observed that adjacent plate

elements can amplify their out-of-plane deflection mutually if the plates have a similar slenderness.

In summary, the studies into wrinkling in RDM demonstrate that wrinkling models should incorporate the plate slenderness, the section and mandrel geometry, and the section and mandrel material properties. They further demonstrate that it is important to align (the velocities of) the machinery and the curved product.

Whereas RDB is used to manufacture a product with a localized curvature, TPRB is often used to provide a product with a curvature over a certain (or the entire) length. A standard TPRB configuration is given in Fig. 2 and consists of the following elements: (1) a first roll, (2) a last roll and (3) a centre roll. TPRB resembles a multi-stage process: The section is placed in between the rolls (see the top left of Fig. 2), succeeded by a uniaxial displacement y_{load} of the centre roll, being the loading phase and providing the section with an initial curvature (see the top right of Fig. 2). Subsequently, the first, centre and last rolls perform rotational movements ω_{fi}, ω_{cr}, and ω_{la}, respectively, causing the section to be fed through the machine in the feeding phase, at the same time being curved over the length, see Fig. 2 at the bottom. The process ends with an unloading phase, in which the product is released from the set-up.

Wrinkling in TPRB has received less attention from the international research community compared to wrinkling in RDB. Shim et al. [18] studied wrinkling of steel RHS during TPRB by using a combined experimental, analytical and numerical approach for a double-stage curving process. A double-stage curving process involves a section, bar or sheet bent to its final radius by feeding it twice through the TRRB configuration; the last time in opposite direction and with an increased displacement y_{load} of the centre roll. The two feeding stages are referred to as the pre-bending and final bending stage, respectively.

The study of Shim et al. [18] was aimed at the determination of the critical pre-bending radius. Also, studies were the effect of pre-bending on the wrinkles observed after the final bending stage. Depending on the difference between the critical radius and the final radius, it was found that pre-bending reduces or prevents wrinkling in the final bending stage. The critical pre-bending radius was predicted by equating the out-of-plane component of the internally developed force due to bending, and the elastic resistance at the onset of yielding. The critical pre-bending radius $R_{\text{crit; pb}}$ follows from:

$$R_{\text{crit;pb}} \geq \frac{3b^2}{2t} \tag{5}$$

where b and t are the width and thickness of the plate element susceptible to wrinkling, respectively.

Different from [18], the TPRB configuration studied in this paper is equipped with additional tooling, consisting of a mandrel and a push unit, see Fig. 3a. This additional tooling does not allow for multi-stage bending. Instead, the section is bent to the required radius in a single stage. The mandrel is a flexible filling, made fit to the interior of the section with practically no initial tolerance. It therefore prevents damage to the section that might otherwise occur as a result of large forces at the location of the centre roll, and possibly also reduces inward wrinkling.

Figure 4 shows the forces exerted on the section. Since the mandrel is made fit to the interior of the section, a frictional force F_{mandrel} develops, causing a friction stress $\sigma(x_{\text{BR}})_{\text{fric}}$ in the section. A pulling-rod transfers the frictional force to the support. This friction often exceeds the slip force between the section and the rolls responsible for feeding the section through the machine. Consequently, the friction hinders or prevents the transport of the section through the bending configuration. A push unit is therefore applied to compensate the additional friction. It exerts a uniaxial actuated movement x_{push} that pushes the section through the machine. The accompanying force F_{push} results into a stress σ_{push} in the section. Friction between the section and the rolls is negligibly small compared to the friction between the section and the mandrel, because of the actuated rotation of the rolls being aligned with x_{push}. Bending and frictional stresses are therefore (amongst others) a function of location x_{BR}, where $x_{\text{BR}} = 0$ refers to the location of first-roll-contact and $x_{\text{BR}} = L$ refers to the last contact point of the TPRB-configuration with the extrusion, with thus, L the total length of the bending region (BR), after which the remaining stress in the section is a residual stress $\sigma_{\text{res.}}$

Wrinkles develop in two stages in the TPRB process. In the first stage, the buckling stage is the part of the compressed plate buckles in front of the centre roll as shown in Fig. 3b. In the second stage, the wrinkling stage, the buckle is reshaped (set) between the centre roll and the mandrel. This paper aims at predicting the largest radius at which buckling occurs during TPRB including a mandrel and a

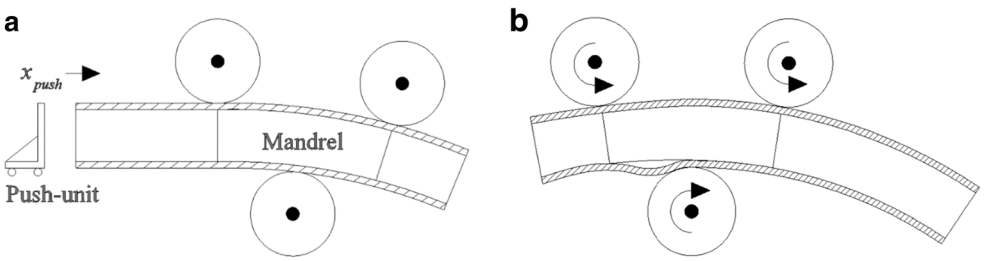

Fig. 3 TPRB process: **a** configuration with push unit and mandrel; **b** plate buckling during TPRB

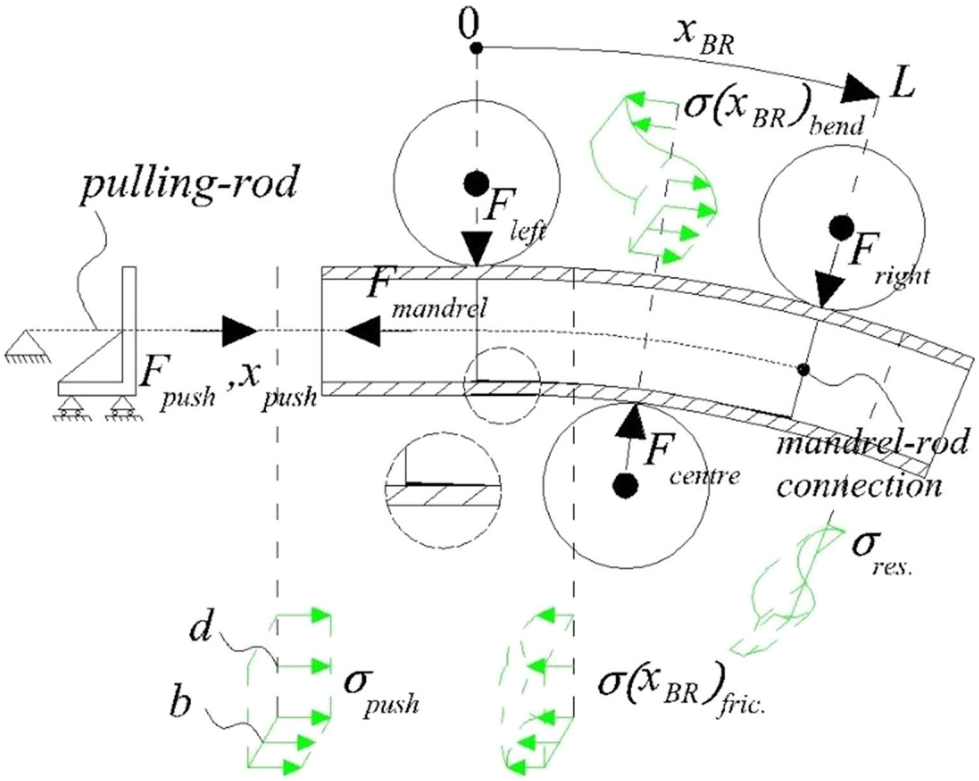

Fig. 4 Set-up during the feeding stage with schematic reaction forces and stresses in the section (the detail in the dotted lined circle shows a possible small gap between section and mandrel)

push unit. An analytical model is employed for this first stage, as elaborated in Section 2. The model is validated with a numerical model using the finite element method (FEM), Section 3. The numerical model is also used to study the second stage of the wrinkling process and this stage is validated by an experiment. The parameters that appeared important for RDB as listed above are incorporated in the study, but sometimes in a simplified fashion. The models presented allow for further extension with additional parameters. Finally, conclusions are given in Section 4. Figure 5 presents the structure of the paper.

2 Analytical description of buckling

This section provides an analytical approach to describe buckling during the loading phase of the compressed plate in front of the centre roll (the first stage of wrinkling development), which is a prerequisite for wrinkling and an upper bound approximation for the critical radius. In this loading phase, the possible beneficial effects of the boosting velocity caused by the push unit (Li et al. [5] and Li et al. [16]) are not yet present and it is therefore the decisive phase for the occurrence of buckling. Shim et al. [18] derived a relationship between the out-of-plane component of the internally developed normal force due to bending and the onset of wrinkling, see Eq. (5). Instead, the current study suggests a theory for the buckling of plate elements of a RHS based on the concept of a semi-infinite section, see Fig. 6, in which it is assumed that the plate element, '*a*' is in-plane supported by the adjacent plate parts '∞.' This theory is used because Shim et al. [18] studied the phenomenon of unrestrained inward wrinkling, whereas it is assumed here that the mandrel fits so tightly that this wrinkling mode is not possible.

Plate element '*a*,' subject to out-of-plane deformation due to buckling, is adjoin with the supporting plate parts '∞,' in which the out-of-plane deformations gradually dissolve. The plate parts adjacent to part '*a*' are referred to as '∞,' because the

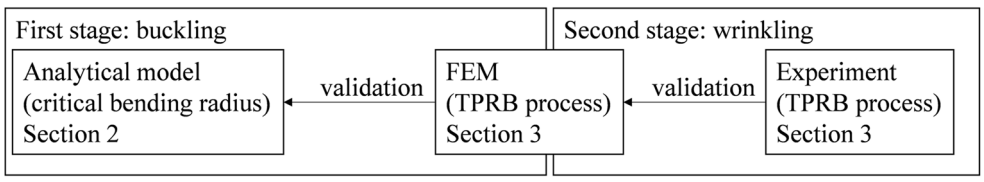

Fig. 5 Paper outline

Analytical model, FEM, and experiment include: TPRB set-up, process parameters, section geometry, boundary conditions, elastic and plastic material properties

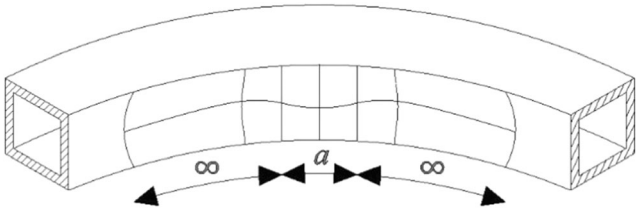

Fig. 6 Semi-infinite section

mechanical behaviour of these parts in combination with practical dimensions allows for the approximation that these plate parts are of infinite length. This statement will be proven below.

As mentioned earlier, He et al. [2] proposed a criterion to predict wrinkling during RDB curving based on the energy method [9], as was shown in Eg. (1). A modification of the denominator of Eq. (1) is considered here to allow for the description of buckling during TPRB:

$$U_{\min} = V + \sum K_{\text{springs}} \tag{6}$$

The terms contributing to the Strain Energy (SE) of the system are the SE of the plate part '*a*,' defined as *V*, and the SE of springs within the system, defined by K_{springs}, which represent the boundary conditions of the plate. These contributions are elaborated hereafter.

2.1 Strain energy of a plate elastically restrained against rotation

Plate element '*a*' is modelled as a plate that is elastically restrained at its edges perpendicular to its width *a*. As a first approach to the problem, a general solution for a plate that is elastically restrained against rotation along its circumference is explored, as shown by the mechanical scheme as given in Fig. 7.

The SE of the plate equals:

$$V = \frac{D}{2}\int_0^b\int_0^a \left(\frac{\partial^2 w}{\partial x^2}\right)^2 + \left(\frac{\partial^2 w}{\partial y^2}\right)^2 + 2\nu\frac{\partial^2 w}{\partial x^2}\frac{\partial^2 w}{\partial^2 y^2}V + 2(1-\nu)\left(\frac{\partial^2 \mathrm{w}}{\partial x \partial y}\right)^2 dxdy \tag{7}$$

where *D* is the flexural rigidity of the plate, *a* and *b* are the plate dimensions, *v* is Poisson's ratio, and *w* is the shape

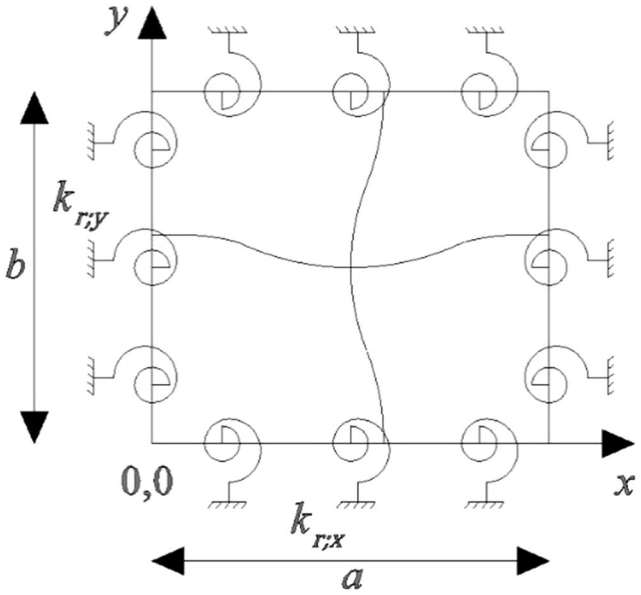

Fig. 7 Elastically restrained plate

function of the deflection. The flexural rigidity of the plate is given by:

$$D = \frac{Et^3}{12(1-\nu^2)} \tag{8}$$

where *E* is Young's modulus and *t* is the plate thickness. The SE of the rotational springs equal:

$$\sum K_{\text{springs}} = 2\left\{\frac{1}{2}\int_0^a k_{r;x}\left(\frac{\partial w}{\partial y}\right)^2 dx\right\} + 2\left\{\frac{1}{2}\int_0^b k_{r;y}\left(\frac{\partial w}{\partial x}\right)^2 dy\right\} \tag{9}$$

where $k_{r;\,x}$ and $k_{r;\,y}$ are the rotational spring stiffness per unit length along the edges aligned with the *x*- and *y*-axis, respectively. Henceforward, the problem is reduced to find (an approximation of) the shape function *w*, and the spring stiffnesses $k_{r,\,x}$ and $k_{r,\,y}$.

2.2 Elastic restrained plates

Qiao and Shan [19] provide a shape function for the out-of-plane deflection of a plate with elastically restrained edges:

$$w(x,y) = \Omega\left\{(1-\psi)sin\left(\frac{\pi x}{a}\right) + \psi\left(1-cos\left(\frac{2\pi x}{a}\right)\right)\right\}\cdot\left\{(1-\vartheta)sin\left(\frac{\pi y}{b}\right) + \vartheta\left(1-cos\left(\frac{2\pi y}{b}\right)\right)\right\} \tag{10}$$

where Ω is the amplitude and ψ and ϑ represent weight factors for the amount of edge restraint about the *y*- and *x*-axis, respectively: A weight factor of zero resembles simply supported edges, whereas a weight factor equal to unity resembles a fully clamped edge.

Realistic values for ψ and ϑ can be obtained by taking into account the dynamic boundary conditions at the elastically restrained edges:

$$M_{y;0} = -D\left.\frac{\partial^2 w}{\partial x^2}\right|_{x=0} = -k_{r;y}\left.\frac{\partial w}{\partial x}\right|_{x=0} \tag{11}$$

$$M_{y;a} = -D\left.\frac{\partial^2 w}{\partial x^2}\right|_{x=a} = k_{r;y}\left.\frac{\partial w}{\partial x}\right|_{x=a} \tag{12}$$

$$M_{x;0} = -D\left.\frac{\partial^2 w}{\partial y^2}\right|_{y=0} = -k_{r;x}\left.\frac{\partial w}{\partial y}\right|_{y=0} \tag{13}$$

$$M_{x;b} = -D\left.\frac{\partial^2 w}{\partial y^2}\right|_{y=b} = k_{r;x}\left.\frac{\partial w}{\partial y}\right|_{y=b} \tag{14}$$

The weight factors are then obtained by substitution of Eq. (10) into the boundary conditions for $M_{y;\,i}$ and $M_{x;\,i}$:

$$\psi = \frac{ak_{r;y}}{ak_{r;y} + 4\pi D} \tag{15}$$

$$\vartheta = \frac{bk_{r;x}}{bk_{r;x} + 4\pi D} \tag{16}$$

The resulting equations illustrate that the amount of edge restraint is a function of the plate dimensions, rotational spring stiffness and the plates' flexural rigidity.

A general solution for the SE as a function of the deflection of a plate with a fully elastically restrained circumference was derived in the Section 2.1. To make this general solution applicable to the current problem, Eq. (10) is modified by considering the boundary conditions that apply during the TPRB process. The plate elements adjacent and perpendicular to the wrinkled plate (shown on the left in Fig. 8 as horizontal flanges at the top and bottom) are free to deflect out-of-plane in the theoretical case of an unrestrained section. However, the mandrel and the roll, including its upper and lower flanges, restrain this out-of-plane deflection for the TPRB process studied here, shown in the centre of Fig. 8. Consequently, the value of the spring stiffness $k_{r;\,x}$ can be regarded as infinite and the clamping ratio ϑ becomes:

$$\vartheta = \lim_{k_{r;x}\to\infty} \frac{bk_{r;x}}{bk_{r;x} + 4\pi D} = 1 \tag{17}$$

Substitution the value $\vartheta = 1$ into Eq. (10) yields:

$$w(x,y) = \Omega\left\{(1-\psi)\sin\left(\frac{\pi x}{a}\right) + \psi\left(1-cos\left(\frac{2\pi x}{a}\right)\right)\right\}\cdot\left\{\left(1-\cos\left(\frac{2\pi y}{b}\right)\right)\right\} \tag{18}$$

Substituting Eq. (18) into Eq. (7) and (9) and subsequently into Eq. (6) yields:

$$U_{\min} = \left(\frac{D\pi^3\left(I_1a^4 + I_2b^4 + I_3a^2b^2\right)}{24a^3b^3} + \frac{3\pi^2k_{r;y}b(\psi-1)^2}{2a^2}\right)\Omega^2 \tag{19}$$

where the terms I_i are given by:

$$I_1 = 48\pi - 96\pi\psi + 512\psi + 192\pi\psi^2 - 512\psi^2 \tag{20}$$

$$I_2 = 9\pi - 18\pi\psi + 96\psi + 153\pi\psi^2 - 96\psi^2 \tag{21}$$

$$I_3 = 24\pi - 48\pi\psi + 256\psi + 120\pi\psi^2 - 256\psi^2 \tag{22}$$

All terms in Eq. (19) apart from spring stiffness $k_{r;\,y}$ have now been defined. A Levy-type plate bending solution is explored as an approach to determine this rotational spring stiffness. This analytical method uses a single Fourier series to describe bending problems for rectangular plates having two opposite simply supported edges and two opposite edges with arbitrary boundary conditions [20]. A Levy-type solution assumes the following displacement function for the plate deflection:

$$\widetilde{w}(x,y) = \sum_{m=1}^{\infty} f_n(x)\sin\left(\frac{\pi my}{b}\right) \tag{23}$$

where $f_n(x)$ is a function (yet to be determined) that describes the deflection in the x-direction and m is the number of half sine waves. Substitution of Eq. (23) into a basic equation for the linear theory of plate bending [21] yields the general Levy-type solution:

$$\widetilde{w}(x,y) = \sum_{m=1}^{\infty}\left\{\frac{\pi mx}{b}\left(A_1\sinh\left(\frac{\pi mx}{b}\right) + A_2\cosh\left(\frac{\pi mx}{b}\right)\right) + A_3\sinh\left(\frac{\pi mx}{b}\right) + A_4\cosh\left(\frac{\pi mx}{b}\right)\right\}\sin\left(\frac{\pi my}{b}\right) \tag{24}$$

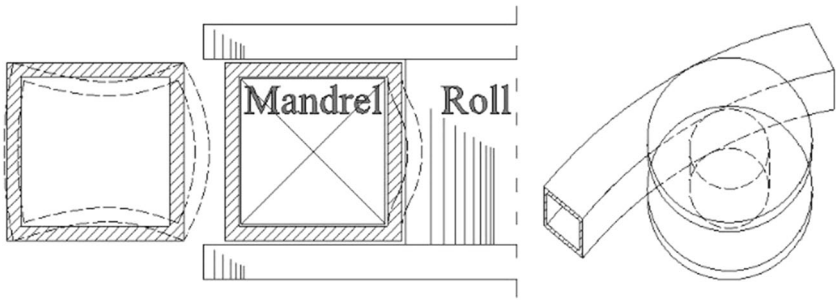

Fig. 8 Restraining properties of the mandrel and roll, including its upper and lower flanges

The terms A_i are constants that depend on the boundary conditions of the plate edges in y-direction, and are based on the system as given by the continuous lines in Fig. 9. In this figure, a_∞ is the width of the supporting plate part "∞", d is the depth of the RHS, and M_0 is a dummy edge moment applied to derive the spring stiffness provided by plate part '∞.'

Although a mandrel is present, inward out-of-plane deflection of plate part '∞' may take place due to a small gap emerging (dotted circle in Fig. 4) at the end of the mandrel. This gap is related to the mandrel stiffness and the dimensional tolerances required to fit the mandrel into the RHS. Because buckling may be related to even small out-of-plane deflections, this potential inward deflection has to be taken into account. It is assumed that the edges of the supporting part aligned with the x-axis, see Fig. 9, are simply supported. Further kinematic and dynamic boundary conditions are:

$$\widetilde{w}\Big|_{x=0} = \widetilde{w}\Big|_{x=a_\infty} = \frac{d^2\widetilde{w}}{dx^2}\Big|_{x=0} = 0 \tag{25}$$

and the dynamic boundary condition related to the dummy edge moment equals:

$$D\frac{d^2\widetilde{w}}{dx^2}\Big|_{x=a_\infty} = -M_0 \tag{26}$$

By substitution of the general Levy-type solution into the boundary conditions, the constants A_i are obtained:

$$A_1 = A_4 = 0 \tag{27}$$

$$A_2 = -\frac{A_3 b\sinh\left(\frac{\pi m a_\infty}{b}\right)}{\pi m a_\infty \cosh\left(\frac{\pi m a_\infty}{b}\right)} \tag{28}$$

$$A_3 = -\frac{a_\infty b\cosh\left(\frac{\pi m a_\infty}{b}\right)}{2\pi m D\sinh\left(\frac{\pi m a_\infty}{b}\right)^2}\sum_{m=1}^{\infty}\frac{4M_0\sin\left(\frac{\pi m}{2}\right)^2}{\pi m} \tag{29}$$

Substitution these terms into Eq. (24) yields the shape function as given in Fig. 10, and this shape is as expected for a plate subjected to an edge moment at $x = a_\infty$.

The value of the rotational spring stiffness of the plate part 'a_∞' can now be obtained by the following relations:

$$\frac{d\widetilde{w}}{dx} = \varphi \tag{30}$$

$$k_{r;y} = \frac{M_0}{\varphi} \tag{31}$$

Combining the latter two equations yields a function for the spring stiffness of the supporting plate element at the edge $x = a_\infty$:

$$\mathrm{k}_{r;y}(y)\big|_{x=a_\infty} = \frac{\pi^2 D\sinh(\boldsymbol{\varkappa})^2}{2\sin\left(\frac{\pi y}{b}\right)\left(b\cosh(\boldsymbol{\varkappa})\sinh(\boldsymbol{\varkappa}) - \mu\cosh(\boldsymbol{\varkappa})^2 + \mu\sinh(\boldsymbol{\varkappa})^2\right)} \tag{32}$$

where

$$\boldsymbol{\varkappa} = \frac{\pi a_\infty}{b} \tag{33}$$

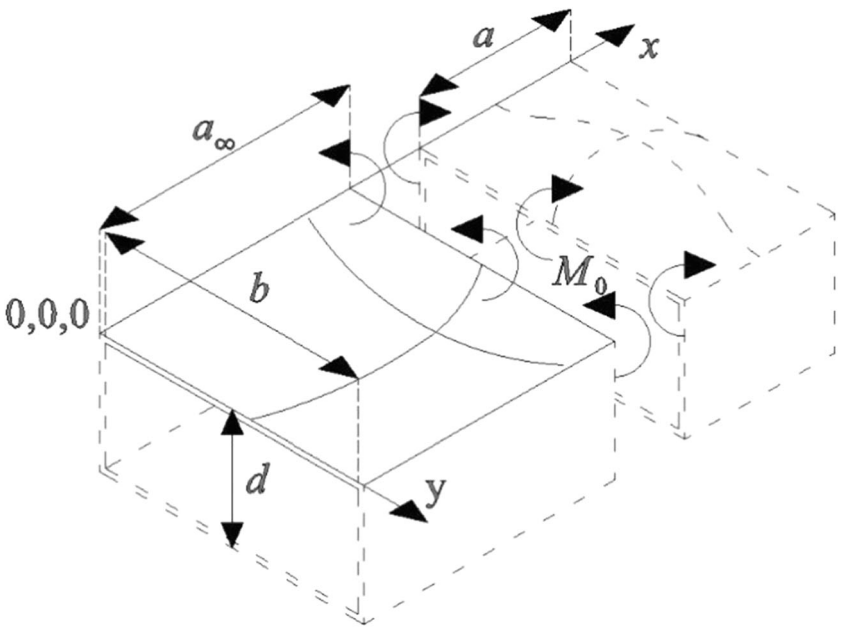

Fig. 9 Part of the RHS section as also shown in Fig. 6

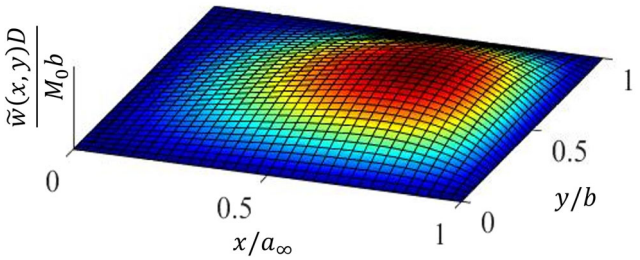

Fig. 10 Deflection field of the supporting plate element

$$\mu = \pi a_\infty \tag{34}$$

However, the value of a_∞ is undefined yet. Thanks to the distance between the rolls in practice, $a_\infty \gg b$. Two extreme cases are therefore considered, namely $a_\infty = b$ and $a_\infty = \infty$. Figure 11 shows the spring stiffness following these extremes, and it can be concluded that the spring stiffness is insensitive to the actual value of a_∞ within the practical domain of TPRB.

Henceforward, the value of $a_\infty = \infty$ is selected, which implies that the plate subjected to local buckling during TPRB is supported by a semi-infinite section. By taking the limit of Eq. (32) with this selected value, the equation for the rotational spring stiffness at the edge $x = a_\infty$ in Fig. 11 becomes:

$$\lim_{a_\infty \to \infty} k_{r;y}(y)\big|_{x=a_\infty} = \frac{\pi^2 D}{2b\sin\left(\frac{\pi y}{b}\right)} \tag{35}$$

Figure 11 further indicates that the value for $k_{r;\,y}$ naturally is low at midspan and shows asymptotic behaviour towards $y = 0$ and $y = b$, where the plate is connected to the other parts.

2.3 Load potential

The SE of the plate has now been obtained; however, also, the load potential (LP) is needed. The LP in [2] considers the potential energy of the load via a numerical model. However, in order to obtain a fully analytic solution, here an analytical approach is used for the LP of a distributed line load as given in [9]:

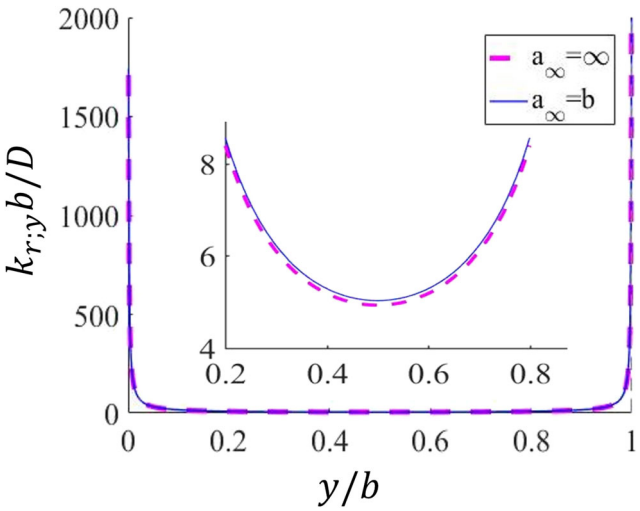

Fig. 11 Rotational spring stiffness of the supporting plate element

$$T = \frac{N_{xx}}{2}\int_0^b\int_0^a \left(\frac{\partial w}{\partial x}\right)^2 dxdy + \frac{N_{yy}}{2}\int_0^b\int_0^a \left(\frac{\partial w}{\partial y}\right)^2 dxdy \tag{36}$$

where N_{xx} and N_{yy} are the loads working in the x- and y-directions (Fig. 9) on the plate respectively. The load $N_{xx} = t\sigma_{xx}$ is a consequence of the stress in the compressed plate between the first and the centre roll. The loading phase—with an actuated movement y_{load} (Fig. 2)—appears to generate the largest compression load during the process, and the accompanying plate load is easily obtained from y_{load}. The plate load N_{yy} is equal to zero for the case here. By substitution of Eq. (18) into Eq. (36) and evaluation of the integral, it follows:

$$T = \frac{\pi I_4 \sigma_{xx} t b}{8a}\Omega^2 \tag{37}$$

In which I_4 is given by:

$$I_4 = 3\pi - 6\pi\psi + 32\psi + 15\pi\psi^2 - 32\psi^2 \tag{38}$$

2.4 Elastic critical buckling stress

The boundary value of 0.8 in Eq. (1) as proposed in [2] takes into account practical conditions during RDB. Because TPRB is a fundamental different curving procedure, the value of 0.8 and the practical conditions on which it is based are questionable for the current application. A theoretical framework is proposed here, so that the upper bound solution of Eq. (1) applies, and $T = U_{\min}$. Namely, to obtain equilibrium for a buckling problem in particular, the SE can be set equal to the load potential (LP), but note that for a normal non-buckling elastic problem, the sum of LP and SE has to be made stationary to find equilibrium. By setting equal the SE in Eq. (19) to the LP in Eq. (37), and defining the stress as the elastic critical stress i.e. $\sigma_{xx} = \sigma_{cr}$, it follows:

$$\frac{\frac{\pi I_4 \sigma_{cr} t b}{8a}\Omega^2}{\left(\frac{D\pi^3\left(I_1 a^4 + I_2 b^4 + I_3 a^2 b^2\right)}{24a^3 b^3} + \frac{3\pi^2 k_{r,y} b(\psi-1)^2}{2a^2}\right)\Omega^2} = 1 \tag{39}$$

All required terms in Eq. (39) for solving σ_{cr} are known, except for the value for a. Therefore, Eq. (39) can be written as:

$$\sigma_{cr} = k_\tau \frac{D}{t} \tag{40}$$

where k_τ is a factor depending on the plate aspect ratio $\tau = a/b$. The critical aspect ratio is obtained by solving:

$$\frac{dk_\tau}{d\tau} = 0 \tag{41}$$

Noting that $\tau > 0$ and $\tau \in \mathbb{R}$, and for the boundary conditions of the plate considered, numerical solving Eq. (41) yields $\tau = 0.91$ or $a = 0.91b$, which agrees with photos of the buckling mode in [18]. Substituting this value together with the expression of $k_{r;\,y}$ in Eq. (15) provides $\psi = 0.596$. The elastic critical stress then follows from Eq. (39):

$$\sigma_{cr} = 102.609\frac{D}{b^2 t} \tag{42}$$

2.5 Elasto-plastic and plastic buckling

Characteristic for TPRB is the continuous process of (plastically) deforming a section in between the rolls. Hence, buckling during TPRB takes place outside the fully elastic regime: $\sigma_{cr} > \sigma_p$ where σ_p is the proportionality stress i.e. the stress at which the material deviates from Hookes law. Stowell [22] derived equations for the critical inelastic buckling stress, $\sigma_{cr,\,inel}$, which consider the influence of the inelastic stress-strain relationships during buckling. As such, Eq. (42) is replaced by:

$$\sigma_{\mathrm{cr,inel}} \leq 102.609\frac{D_p}{b^2 t}\xi_c \tag{43}$$

where D_p is the flexural rigidity of the plate in the inelastic regime, defined hereafter, and ξ_c takes into account the reduced stiffness in the inelastic regime. For the specific case of the boundary conditions of the current plate, [22] provides:

$$\xi_c = \frac{E_s}{E}\left(0.352 + 0.648\sqrt{\frac{1}{4} + \frac{3}{4}\frac{E_t}{E_s}}\right) \tag{44}$$

in which E_s and E_t are the secant and tangent modulus, respectively:

$$E_s = \frac{\sigma}{\varepsilon(\sigma)} \tag{45}$$

$$E_t = \left(\frac{d\varepsilon(\sigma)}{d\sigma}\right)^{-1} \tag{46}$$

where ε is the strain and σ is the stress. Hence, the values for E_s and E_t follow from the stress-strain curve. A widely applied stress-strain model for aluminium alloys is the Ramberg-Osgood model, [23]:

$$\varepsilon(\sigma) = \frac{\sigma}{E} + \varepsilon_0\left(\frac{\sigma}{f_0}\right)^n \tag{47}$$

where ε_0 is the permanent 0.2% strain i.e. $\varepsilon_0 = 0.002$, f_0 is the 0.2% proof stress of the alloy considered, and n is the strain hardening index of the alloy. Equation (43) can be replaced by a two-branch model for a better resemblance of test results [23]:

$$\varepsilon(\sigma) = \begin{cases} \frac{\sigma}{E} + \varepsilon_0\left(\frac{\sigma}{f_0}\right)^{n_1} & \text{if } \sigma \leq f_0 \\ \frac{\sigma}{E} + \varepsilon_0\left(\frac{\sigma}{f_0}\right)^{n_2} & \text{if } \sigma > f_0 \end{cases} \tag{48}$$

Also Poisson's ratio changes when $\sigma > \sigma_p$. Taking into account incompressibility in the fully plastic regime, this ratio in Eq. (8) is replaced by the coefficient of lateral contraction v_p [24]:

$$v_p = \frac{1}{2}\left(1 - (1-2v)\frac{E_t}{E}\right) \tag{49}$$

Furthermore:

$$D_p = \frac{Et^3}{12\left(1-{v_p}^2\right)} \tag{50}$$

Hence, Eq. (43) takes into account the change in stiffness and lateral contraction of the material during strain hardening. Equation (48–50) can be solved numerically, and the critical strain, ε_{cr}, then follows from Eq. (48). Finally, the critical bending radius at the neutral axis R_{crit} follows from the compatibility equation:

$$k = \frac{1}{R_{\mathrm{crit}}} = \frac{2\varepsilon_{\mathrm{cr}}}{d} \tag{51}$$

Figure 12 shows this critical bending radius vs. the plate slenderness for a RHS with dimensions and material properties according Table 3. The material data is obtained via coupon tests on alloy AA 6063-T6. It appears that the ratio between the critical radius and the squared slenderness is almost constant, which corresponds to practical experience as given by TPRB operators.

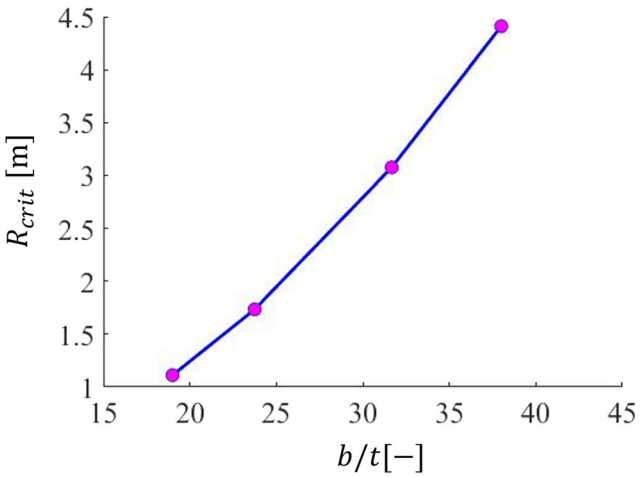

Fig. 12 Critical radius vs. slenderness for an RHS with Table 3 properties

Table 3 Geometric and material properties of the RHS applied in the simulations

b [mm][a)]	d [mm][a)]	t [mm]	E [GPa]	$f_{0.2}$ [MPa]	f_u[b)] [MPa]	n_1[-]	n_2 [-]
$100-2t$	$50-2t$	2.5–5.5	70	150	195	11	18

[a)] Outer dimensions of the section are 100 mm × 50 mm

[b)] f_u= ultimate tensile strength, provided here for reference

3 Finite element simulations

The previous section provides the means to predict local elasto-plastic buckling during TPRB. Although buckling is a required precursor for wrinkling, it cannot describe the wrinkling pattern that may be found after TPRB. Just before wrinkling, an initial buckle comes into contact with the centre roll and possibly with the mandrel as shown in Fig. 13. This contact causes a shape transformation from a buckling mode to a wrinkling pattern. This transformation process depends on the loading history of the material, cross-sectional properties, several contact parameters and machine settings. In turn, contact parameters depend on the COF and the stiffness and geometry of the parts. Consequently, an analytic approach to predict wrinkling is believed to be almost impossible, and therefore, the FEM is used instead. Simulations are performed with ABAQUS version 6.14.

3.1 Geometry and materials

The geometry and material selected for the FE simulations are identical to those used for Fig. 12 i.e. following the values according to Table 3, and with a wall thickness t equal to 3 mm. Table 4 provides the specifications of the machinery. A bending radius was selected such that wrinkles could be expected that are visible to the naked eye. Figure 14 shows the components included in the FE model, and Table 5 describes the approach followed to model them. The first and last rolls are modelled as rigid bodies to reduce computational time. The centre roll is modelled as a ring instead of a solid disc—i.e. the core is omitted— to reduce the number of elements. These aforementioned components are significantly stronger and stiffer than the section and mandrel, and hence, simplifying these components is not expected to reduce the accuracy.

Shim et al. [18] used Abaqus S4R shell elements to simulate the RHS in the TPRB process. For the current application, however, these reduced integrated four node shell elements, with only one integration point over the surface, suffered from shear locking. Therefore fully integrated four-noded S4 shell elements were used, which performed well.

It follows from Eq. (18) and the semi-infinite-section and the bucking mode found by Shim et al. [18] that the first buckling mode is symmetrical for the geometry concerned and has an Eigenvalue that is significantly lower than those of the second and successive Eigenmodes. For this reason, only half of the TPRB configuration is modelled, using symmetry conditions along the symmetry axis. All possible contact areas are defined as surface-to-surface contacts. The contact formulations are based on Abaqus-specific hard contact and penalty friction. The COF's are selected based on practical experience of TPRB operators and are given in Table 6.

As mentioned in the introduction, a standard TPRB process comprises of three phases, being the loading phase, the feeding phase and the unloading phase. Furthermore, a TPRB configuration equipped with a push unit requires an actuated angle correction during the loading phase, the so-called AC-phase, in which the configuration of the three rolls is rotated over ω_{corr}, see Fig. 15. This is to ensure alignment of the push

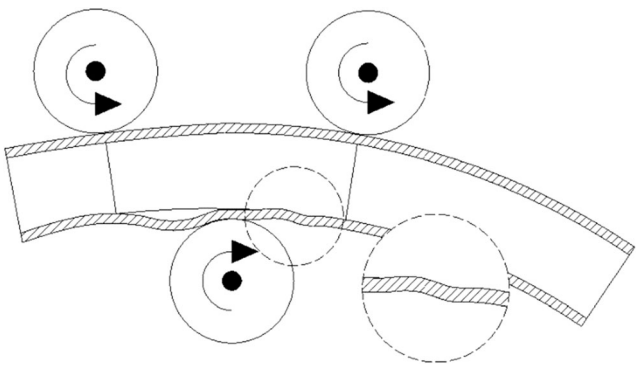

Fig. 13 Buckling and wrinkling (wrinkling detail in the dotted circle) during TPRB

Table 4 Dimensions of the components and machinery

Component	Value [mm]
Roll diameters	200
Centre-to-centre distance between the first and last rolls	700
Centre roll displacement y_{load} (Fig. 2) after tight fit of RHS between rolls	48
RHS[a)]	100 × 50 × 2.5
Mandrel clearance	0.5
Mandrel length	600
Bending radius	805

[a)] Ratio $b/t = (100\text{ mm} - 2 \cdot 2.5\text{ mm})/2.5\text{ mm} = 38$

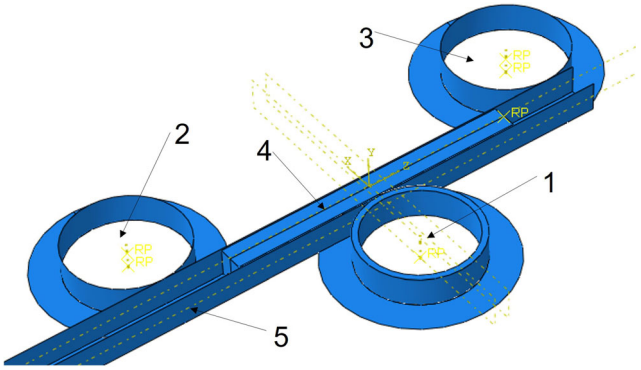

Fig. 14 Geometry of the FE model, see Table 5 for a definition of the numbers

unit with the section. In practice, often, a slightly lower value than strictly required (undercompensation) is applied in order to ensure contact between the RHS and the first roll. Such an undercompensation is also applied in the FE model.

Additional computational effort is required to model the angle correction phase. To avoid simulating this step in the FEM whilst ensuring that the alignment between the RHS and the push unit remains as in practice, the rolls are modelled with a fixed position and instead of a single directional motion of the push unit, v_{push} in Fig. 15, a bi-axial motion is applied with the resultant being perpendicular to the section's cross-section after the loading phase. Figure 16 shows the results, and indeed, the resulting push unit movement is aligned with the length axis of the undeformed part of the RHS.

With respect to the feeding phase, Shin et al. [25] derived a method to predict the required centre roll displacement, y_{load} in Fig. 2, for a certain desired curvature of a plate. Using similar principles, a relation is derived here between the required curvature of the RHS, and the corresponding centre roll displacement y_{load}, the angular velocities of the rolls ω_{fi}, ω_{cr}, and ω_{lr} (Fig. 2) and the corresponding bi-axial movement of the push unit in x- and y-direction, x_{push} and y_{push} respectively, to simulate ω_{corr}. Table 7 provides velocities applied in the FE model for these process parameters to reach their proper relative displacements at the end of the simulation.

Table 5 Components included in the FE model

#	Name	Behaviour	Type of element
1	Centre roll[a)]	Deformable/analytical rigid	Solid/revolved shell
2	First roll	Analytical rigid	Revolved shell
3	Last roll	Analytical rigid	Revolved shell
4	Mandrel	Deformable	Solid
5	RHS	Deformable	Shell

[a)] Material applied: steel grade S235 (yield strength 235 MPa)

Table 6 COF's used in the FE model

Contact	Between components	COF
RHS-rolls	1–5, 2–5, 3–5	$\mu = 0.25$
RHS-mandrel	4–5	$\mu = 0.05$

3.2 Simulation steps and mesh size

A dynamic implicit solution scheme is used, taking into account non-linear geometrical effects and material properties. Mesh densities have been selected as based on a convergence study, taking into account the occurring stress gradients, the final obtained wrinkling shape, and EDPD.

Note that the RHS wall thickness used for the mesh sensitivity study was slightly different from those in the rest of this paper, namely $t = 3$ mm (instead of $t = 2.5$ mm, Table 4). In the convergence study, studied element sizes for the extruded section were approximately 10 × 10 mm, 5 × 5 mm, 3 × 3 mm, and 2 × 2 mm. Figure 17 shows the wrinkles and stress patterns of the simulations for the selected mesh sizes. It can be seen that the wrinkle shape depends on the mesh size. However, the Von Mises equivalent stress has the same magnitude for all simulations, whereas the stress contours and wrinkling shape of the RHS appear to converge with a refinement of the mesh.

As Fig. 17 provides a qualitative comparison of the mesh size, the EDPD is selected as a quantitative criterion to evaluate the mesh size, see Fig. 18. The figure shows that the solution converges slowly with an increased mesh density; however, the computational time increases rapidly with an increasing mesh density, see Fig. 19. Therefore, a mesh size of 2 × 2 mm was selected for further analysis, as a trade-off between accuracy and computational costs. Shim et al. [18] also concluded that a mesh size of 2 × 2 mm is appropriate in their TPBR setup for describing wrinkling of a section of similar size and shape.

To explore the effect of imperfections, a sine-based imperfection field was applied to the compressed plate of the extruded section by:

$$w_{\text{imp}}(x,y) = \Omega_{\text{inp}} \sin\left(\frac{\pi x}{b}\right) \sin\left(\frac{\pi y}{b}\right) \tag{52}$$

in which Ω_{inp} is selected as $b/1000$, which is a typical value for aluminium extrusions [23, 26]. This imperfection field did not influence the results of the FE model, in terms of occurrence and magnitude of the wrinkles. This is attributed to the fact that buckling and deformations enforced by the centre roll are so significant that they outweigh initial imperfections.

3.3 Results of the FE model

For validation purposes, a TPRB test was performed with the same set-up, process parameters, geometry and material

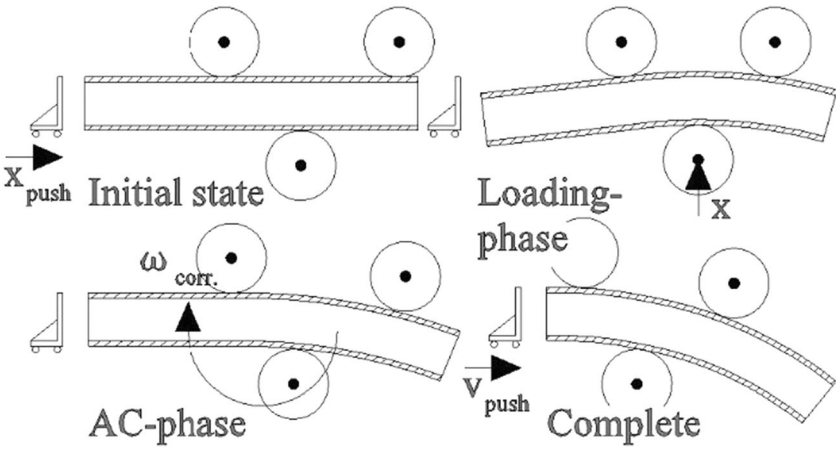

Fig. 15 Steps during TPRB process including a push unit, where the AC-phase rotates the three rolls such that the section end is aligned with the push unit

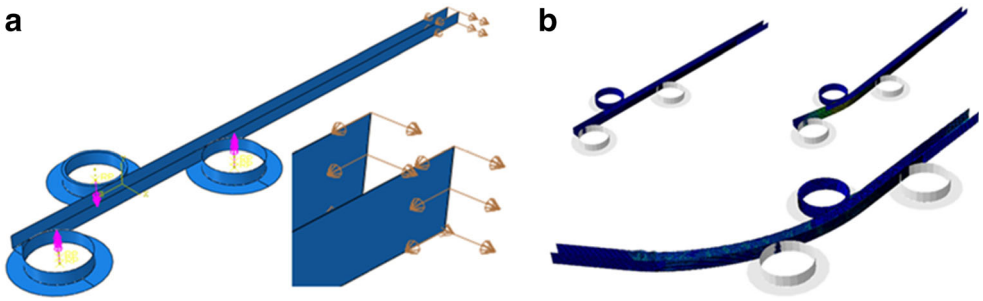

Fig. 16 FE simulation of the TPRB process including a push unit: **a** boundary conditions and load, with brown arrows indicating the push unit movement; **b** three steps during the analysis

Table 7 Process parameters as used in the FE model

Parameter	Value	Step	Time [Sec.]
y_{load}	5 [mm/s]	Loading	9.6
ω_{cr}	0.098 [rad/s]	Feeding	150
$\omega_{fr} = \omega_{lr}$	-0.102 [rad/s]	Feeding	150
x_{push}	10.35 [mm/s]	Feeding	150
y_{push}	1.75 [mm/s]	Feeding	150

properties as applied in the FE model i.e. with values given in Tables 3, 4, and 5 and with the same relative velocities as in Table 7. The material properties in Table 3 were measured by coupon tests from the same RHS as used in the TPRB test. Figure 20 compares the deformations of the RHS in the FE model and the TPRB experiment. The good qualitative

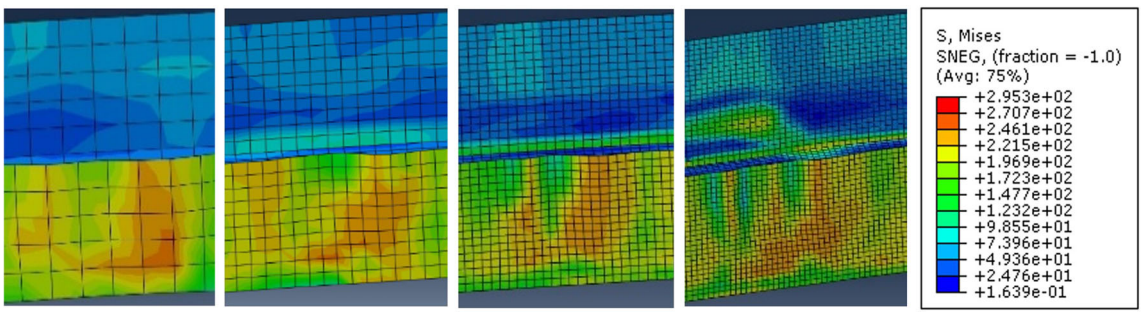

Fig. 17 Mesh size dependent Von Mises stress and wrinkling pattern (left to right: 10 × 10 mm, 5 × 5 mm, 3 × 3 mm, and 2 × 2 mm element size)

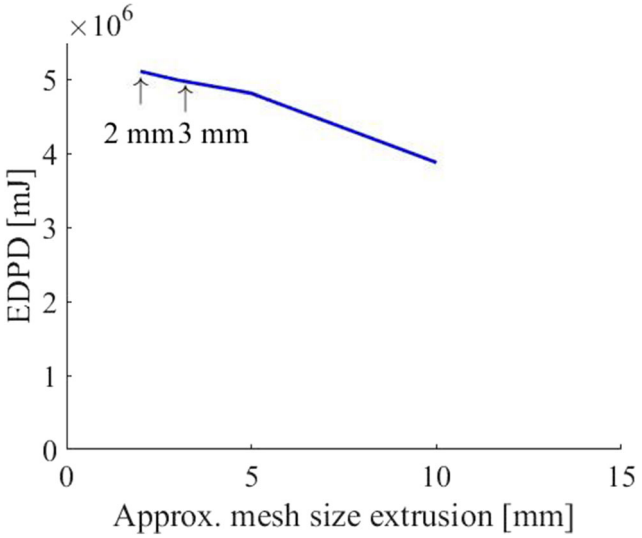

Fig. 18 EDPD as a function of mesh size

agreement of deformations and bent curvature between the test and the FE model indicate the usefulness of the FE model.

Table 8 provides a quantitative comparison between the experiment and the FE model. A good agreement is observed between most of the characteristics. The number of wrinkles per length in the experiment varies, whereas it is regular in the FE simulation. Therefore, it is expected that some of the buckles in the experiment were flattened instead of transferred into wrinkles. The variation in the number of wrinkles per unit length in the experiment is attributed to machine-related geometrical imperfections and eccentricities, causing the RHS to be fed through the machine in an irregular manner. Differently, the FE model simulates perfect TPRB operation, and consequently, a regular wrinkling pattern is obtained.

Figure 21 presents the reaction forces according to the FE model, with definitions given in Fig. 4. The loading phase—

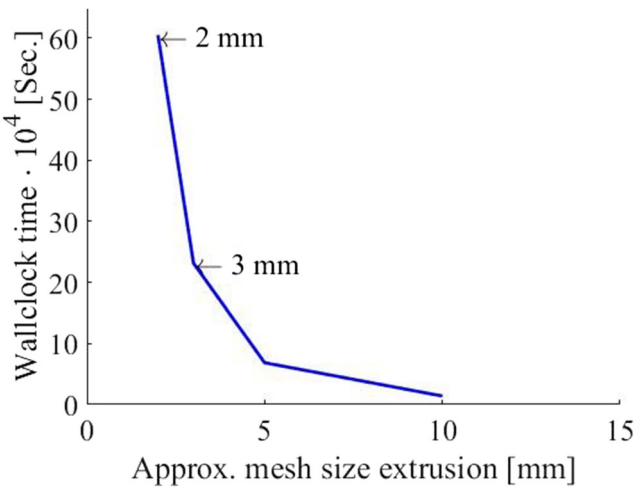

Fig. 19 Wall clock time as a function of mesh size

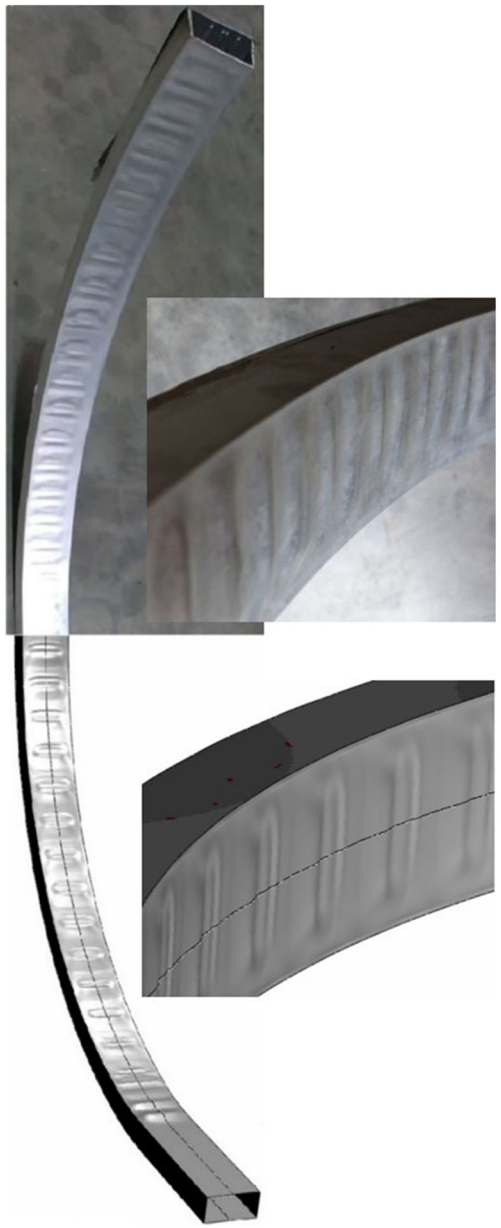

Fig. 20 TPRB wrinkling as obtained by the experiment (top) and in the FE model (bottom)

where the centre roll is displaced with y_{load} with a constant velocity—starts at $t = 0$ and ends at time t_3. The non-linear

Table 8 Wrinkle characteristics of the experiment and the FE model

Characteristic	FE model	Experiment
Wrinkle height	$0.74b$	$0.80b$
Wrinkle width	$0.24b - 0.40b$	$0.23b - 0.33b$
Wrinkle depth	$0.004b - 0.0075b$	$0.009b$
Wrinkles per unit length	$1.35/b$	$1.40/b - 3.65/b$
Number of wrinkles per metre	14.5	16.85[a)]

[a)] Average over the curved part of the section.

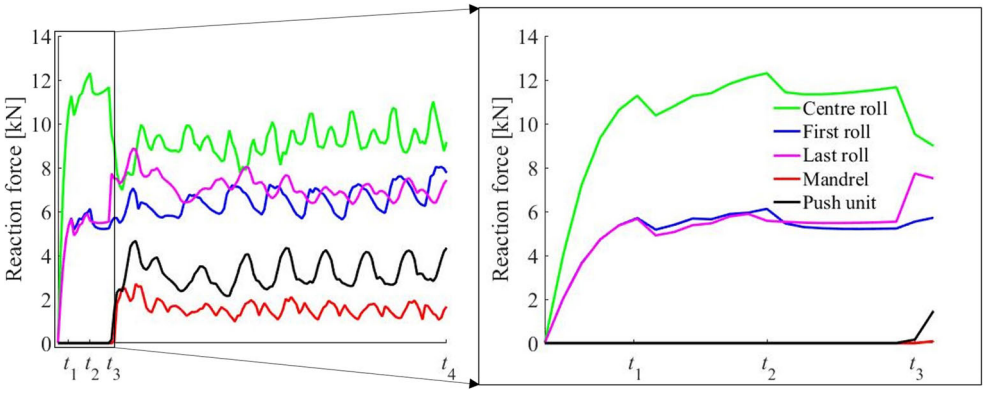

Fig. 21 Resultant reaction forces of the FE model: **a** entire simulation; **b** close up of the loading phase

curve of roll reaction force versus time up to t_1 shows that the RHS deforms plastically. The roll reaction forces reduce at time t_1 caused by inelastic buckling of the RHS. A second buckle develops at time t_2. The push unit is activated with constant velocity at time t_3 i.e. immediately after the loading phase. A push unit force then develops together with the mandrel frictional force. At the same time, the centre roll reaction force decreases whereas the last roll reaction force increases. The fluctuation of the forces during the entire process is caused by the development of buckles and the subsequent contact of buckles against the centre roll. A slight increase over time of the first roll reaction force is visible, which is caused by the undercompensating value of ω_{corr} as shown in Fig. 15. Time t_4 up to which the feeding phase is displayed is halfway the total feeding phase.

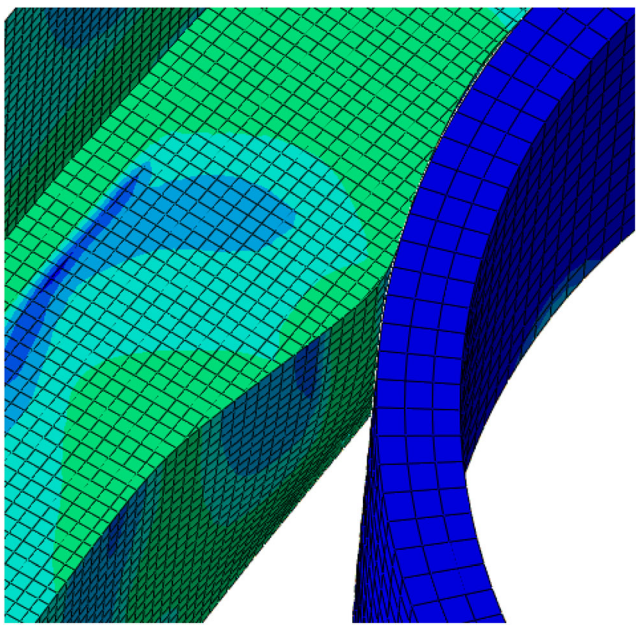

Fig. 22 Plate buckling during TPRB (half model mirrored to show the complete section)

3.4 Comparison between the analytical model and the FE model

The FE model shows a wrinkling pattern quite comparable to the experiment, and is therefore considered useful to predict and validate the analytically derived critical radius. Indeed, the FE model showed that buckling of the extrusion takes place in front of the centre roll, Fig. 22, with a buckling shape a/b that corresponds with the shape derived in Section 2, and with only outwards out-of-plane deformations.

The modelled RHS has a slenderness ratio of $b/t = 38$, see Table 3. As can be obtained from Fig. 12, this corresponds to a critical radius of approximately $R_{crit} = 4.5$ m. To verify this further, two additional FE simulations were made: one with a radius equal to this analytically derived critical radius $R_{TPRB} = R_{crit}$, and one with a 10 % smaller radius $R_{TPRB}=0.9R_{crit}$. The out-of-plane deflection field of the plate susceptible to buckling is shown in Fig. 23 for $R_{TPRB} = R_{crit}$ (left) and for $R_{TPRB}= 0.9R_{crit}$ (right), where R_{TPRB} is the radius induced by the FE TPRB configuration. Figure 23 shows that buckling occurs in the FE model if $R < R_{crit}$ whereas it remains absent for $R = R_{crit}$. This supports the predictive capability of the analytical solution for elasto-plastic plate buckling in TPRB.

4 Conclusions

This paper considered local buckling and wrinkling of a RHS in a three-point-roll bending (TPRB) set-up that includes a push unit and a flexible mandrel. Local buckling and wrinkling were studied both analytically and via simulations, and results were further verified by an experiment. As far as the authors know, this paper presents for the first time Timoshenko's energy method (for buckling: equating strain energy and load potential) in combination with the Ramberg Osgood material model. The following conclusions can be made:

- TPRB processing of RHSs can lead to wrinkling of the fully compressed plate at the inner radius, if the ratio between the

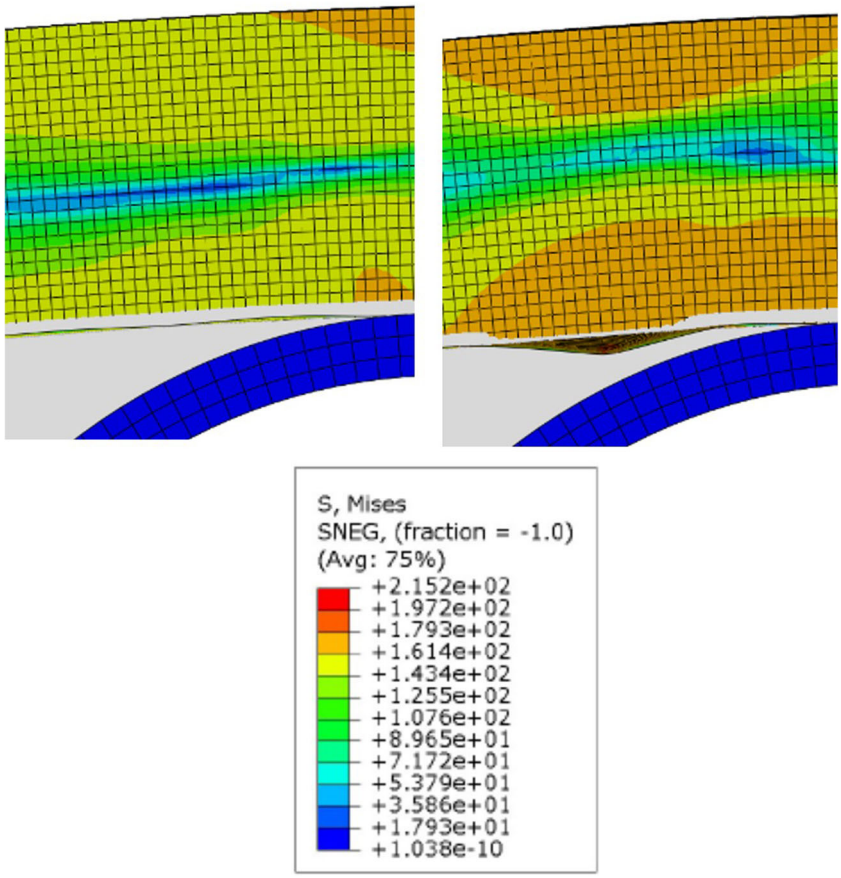

Fig. 23 Numerical simulation of plate buckling during TPRB. Left: simulation with $R_{TPRB} \approx R_{crit}$; right: simulation with $R_{TPRB} \approx 0.9R_{crit}$x

squared plate slenderness $(b/t)^2$ and the curving radius exceeds a certain value, for the studied RHS equal to 0.32 mm^{-1}.

- Wrinkles develop in two stages. For the first stage, buckling of the bent section occurs in front of the centre roll. The analytical model developed herein is capable of predicting the conditions for which this buckling occurs. In addition to traditional plate buckling, the model takes into account elasto-plastic behaviour and the specific boundary conditions. As such, it has been demonstrated that this stage can be predicted with Timoshenko's energy method (for buckling: equating strain energy and load potential) in combination with the Ramberg Osgood material model. Namely, a FE model with the model predicted radius indeed does not show buckling whereas a FE model with a 10% smaller radius does show buckling.
- During the second stage (the wrinkling stage), a present buckle is reshaped between the mandrel and the centre roll, causing the buckle to transform into a wrinkle. This phenomenon appears to depend on contact, material and geometrical properties of the extruded section, as well as on machine settings. Due to its complexity, this phase has here been simulated by a FE model. Good agreement was observed between the FE model and an experiment, comparing the curvature radius and the wrinkling deformations. For example, the experimental wrinkle height of 0.80b was predicted by the FE model to be 0.74b, a very useful result.
- The flexible mandrel, which was made fit to the interior of the RHS such that practically no initial clearance existed, reduces and possibly even prevents inward wrinkling in TPRB. On the other hand, due to the mandrel, longitudinal compression stress in the section increases through friction between the section and the mandrel. For the friction coefficient used here, the net effect of the mandrel is beneficial i.e. it results in a reduction of the curvature radius at which wrinkling occurs.

Acknowledgments Bart Simonse (Kersten Europe) is kindly acknowledged for sharing his experience in TPRB and for providing access to their TPRB machines and materials. Okko Coppejans (TNO) and Roel Spoorenberg (Femtec) are acknowledged for their support in selecting appropriate settings for the FE model.

Authors' contributions RC has performed the FE simulations. The three authors contributed equally to the manuscript.

Compliance with ethical standards

Conflict of interest The authors declare that they have no conflict of interest.

Ethical approval Not applicable.

Consent to participate Not applicable.

Consent to publish Not applicable.

References

1. Zhu X, Ogi K, Okabe N (2019) Study on wrinkles during rotary-draw bending forming. Mater Sci Forum 943:43–47. https://doi.org/10.4028/www.scientific.net/msf.943.43
2. He Y, Jing Y, Mei Z, Heng L, Yongle K (2009) 3D numerical study on wrinkling characteristics in NC bending of aluminum alloy thin-walled tubes with large diameters under multi-die constraints. Comput Mater Sci 45:1052–1067. https://doi.org/10.1016/j.commatsci.2009.01.010
3. Xiao Y, Liu Y, Yang H, Ren J (2013) Optimization of processing parameters for double-ridged rectangular tube rotary draw bending based on grey relational analysis. Int J Adv Manuf Technol 70:2003–2011. https://doi.org/10.1007/s00170-013-5429-4 K . X. L., Shunqi Z., Y. S. Z., Y. C., Y. H
4. Chen J, Daxin E, Zhang J (2013) Effects of process parameters on wrinkling of thin-walled circular tube under rotary draw bending. Int J Adv Manuf Technol 68:1505–1516. https://doi.org/10.1007/s00170-013-4938-5
5. Li H, Liu Y, Zhu Y, Yang H (2014) Global sensitivity analysis and coupling effects of forming parameters on wall thinning and cross-sectional distortion of rotary draw bending of thin-walled rectangular tube with small bending radius. Int J Adv Manuf Technol 74:581–589. https://doi.org/10.1007/s00170-014-6014-1
6. Safdarian R (2019) Experimental and numerical investigation of wrinkling and tube ovality in the rotary draw bending process. Proc Inst Mech Eng C J Mech Eng Sci 233:5568–5584. https://doi.org/10.1177/0954406219850857
7. Fang J, Lu S, Liang C, Zheng D, Wang J (2019) Mandrel role in numerical control rotary draw bending process of TA18 high strength titanium alloy tube. Mater Sci Eng 631:022065. https://doi.org/10.1088/1757-899x/631/2/022065
8. Liang J, Li J, Wang A, Li Y, Liang C (2020) Study on the influence of different cores on section quality in the process of pure rolling rotary draw bending wrinkling of profiles with "日"-shape section. Int J Adv Manuf Technol 110:471–479. https://doi.org/10.1007/s00170-020-05903-9
9. Timoshenko SP, Gere JM (2012) Theory of elastic stability, 2nd edn. McGraw-Hill
10. Li H, Yang H, Zhang Z, Li G, Liu N, Welo T (2014) Multiple instability-constrained tube bending limits. J Mater Process Technol 214:445–455. https://doi.org/10.1016/j.jmatprotec.2013.09.027
11. Li H, Yang H, Zhan M (2009) A study on plastic wrinkling in thin-walled tube bending via an energy-based wrinkling prediction model. Model Simul Mater Sci Eng 17:035007. https://doi.org/10.1088/0965-0393/17/3/035007
12. Jie D, Yuli L, He Y Research on the sensitivity of material parameters to cross-sectional deformation of thin-walled rectangular tube in rotary draw bending process. J Mater Res 31:1784–1792. https://doi.org/10.1557/jmr.2016.194
13. Zhao G, Liu Y, Dong C, Yang H, Fan X (2010) Analysis of wrinkling limit of rotary-draw bending process for thin-walled rectangular tube. J Mater Process Technol 210:1224–1231. https://doi.org/10.1016/j.jmatprotec.2010.03.009
14. Guangjun L, Heng Y, Xudong X, Heng L, He Y (2018) Formability of thin-walled commercial pure titanium tube upon rotary draw bending. Rare Metal Mater Eng 47:26–32. https://doi.org/10.1016/s1875-5372(18)30066-3
15. Hasanpour K, Barati M, Amini B, Poursina M (2013) The effect of anisotropy on wrinkling of tube under rotary draw bending. J Mech Sci Technol 27:783–792. https://doi.org/10.1007/s12206-013-0124-9
16. Li H, Ma J, Liu B, Gu R, Li G (2018) An insight into neutral layer shifting in tube bending. Int J Mach Tools Manuf 126:51–70. https://doi.org/10.1016/j.ijmachtools.2017.11.013
17. Liu K, Zheng S, Zheng Y, Chen Y, He Y (2016) Plate assembly effect and cross-section distortion of rectangular tube in rotary draw bending. Int J Adv Manuf Technol 90:177–188. https://doi.org/10.1007/s00170-016-9283-z
18. Shim DS, Kim KP, Lee KY (2016) Double-stage forming using critical pre-bending radius in roll bending of pipe with rectangular cross-section. J Mater Process Technol 236:189–203. https://doi.org/10.1016/j.jmatprotec.2016.04.033
19. Qiao P, Shan L (2007) Explicit local buckling analysis of rotationally restrained composite plates under biaxial loading. Int J Struct Stab Dyn 07:487–517. https://doi.org/10.1142/s021945540700240x
20. Ventsel E, Krauthammer T (2001) Thin plates and shells. CRC Press, Boca Raton
21. Alfutov NA (2013) Stability of elastic structures. Springer-Verlag, Berlin Heidelberg
22. Stowell ZE (1948) A unified theory of plastic buckling of columns and plates. National Advisory Committee for Aeronautics. Langley Aeronautical Lab, Hampton
23. Mazzolani F (1998) Aluminium alloy structures, 2nd edn. E&FN Spon
24. Chakrabarty J (2010) Applied plasticity, 2nd edn. Springer Science+Business, New York
25. Shin JG, Lee JH, Kim YI, Yim H (2001) Mechanics-based determination of the center roller displacement in three-roll bending for smoothly curved rectangular plates. KSME Int J 15:1655–1663. https://doi.org/10.1007/bf03185120
26. Maljaars J, Soetens F, Snijder HH (2010) Local buckling of fire exposed aluminium members: new design model. J Struct Eng 136:66–75. https://doi.org/10.1061/(asce)st.1943-541x.0000091